Stable Planning through Aligned Representations in Model-Based Reinforcement Learning

Misagh Soltani
Dept. of Computer Science and Engineering
University of South Carolina
Columbia, SC 29201
msoltani@email.sc.edu

Forest Agostinelli
Dept. of Computer Science and Engineering
University of South Carolina
Columbia, SC 29201
foresta@cse.sc.edu

Abstract

Integrating planning with reinforcement learning (RL) significantly improves problem-solving capabilities for sequential decision-making problems, particularly in sparse-reward, long-horizon tasks. Recently, it has been shown that discrete world models can be trained such that no model degradation occurs over thousands of time steps and states can be re-identified during planning. As a result, a heuristic function can be trained with data generated from the world model, and the learned world model and heuristic function can be used with planning to solve problems. However, this approach fails to solve problems with state transformations to which the world model and heuristic function should be invariant (i.e., noise), without re-training the world model and heuristic function. In this work, we introduce Stable Planning through Aligned Representations (SPAR), an efficient framework that trains a discrete world model and heuristic function in a clean Markov decision process (MDP) and trains an alignment network to map transformed states to their discrete latent state in the clean MDP. When solving problems, we exploit the underlying discrete latent representation and round the output of the alignment network with the aim of exactly matching the clean latent state. As a result, adapting to transformations only requires training the adaptation network while the world model and heuristic function remain fixed. We then demonstrate its effectiveness on Rubik's Cube and Sokoban domains, and compare it with applying a similar approach to a world model with continuous latent representations. SPAR successfully solves over 90% of problems with 17 different visual transformations and real-world images. This adaptation process requires no additional world model or heuristic function re-training, and reduces re-training time by at least 95%.

1 Introduction

Many real-world problems require long-horizon planning to find solutions. However, planning cannot happen when the state transition function (also known as the "world model"), which maps states and actions to next states, is not known. One approach used to address this, which has yielded success in both simulation and the real-world, is to learn the world model using data obtained from interacting with the environment [1, 2, 3, 4, 5]. These methods then use the learned world model to train a heuristic function, which either estimates the expected future reward, in the general reinforcement leanring setting, or remaining cost to go to the goal (also known as the "cost-to-go"), in the more restricted pathfinding setting. Given a test instance, the learned world model and heuristic function used with a heuristic search algorithm, such as Monte Carlo tree search (MCTS) [6] or A* search [7]. However, these approaches are not robust no noise. For example, if irrelevant distractors that were not seen during training are part of a state at test time, the learned world model's prediction may

39th Conference on Neural Information Processing Systems (NeurIPS 2025) Workshop: Embodied World Models for Decision Making.

become very unreliable making finding solutions impractical. As a result, these approaches will most likely fail to generalize beyond very carefully controlled settings. Furthermore, when specifying goals with a goal images, noise present in the environment can make goal state identification difficult. For example, if a goal image is specified in a bright room and the room is currently dark, unless the action space includes controlling the lights, there is no sequence of actions that can reach the goal image.

One approach to solving this problem of noise could be to train the world model on noisy states. However, this suffers from the following drawbacks: (1) The world model is forced to capture noisy transitions, which may require more parameters and hinder performance; (2) Goal state identification still depends on the noise present in the state, which means different goal images must be given based on the noise present in the start state; and (3) It requires that the world model and heuristic function be re-trained if a new type of noise is introduced. On the other hand, another approach would begin with training a world model in a clean environment (i.e. without noise). At test time, if noise is present, the data obtained from training the world model is re-used by adding noise to the states and training an alignment model that maps the noisy states to the clean states. As a result, no new data need be obtained and the world model and heuristic function remain fixed. However, one potential drawback of this approach is that small differences in the denoised state and the clean state could cause compounding errors to occur when applying the world model across many timesteps, also known as model-degradation.

To address these issues, we introduce Stable Planning through Aligned Representations (SPAR). SPAR trains a discrete world model that maps states in a clean environment to a discrete latent state and then trains an alignment model to map noisy states to their discrete latent representation in the clean environment. SPAR exploits the fact that the latent representation is discrete by rounding the output of the alignment model when solving problems with the aim of exactly matching the true discrete latent state. Since discrete world models have been shown to accurately predict next states across thousands of timesteps without model degradation [5], this also enables planning over long horizons without model degradation in the presence of noise. On the other hand, we show that training an alignment model for a world model with a continuous latent representation results in model degradation, even when the continuous model does not exhibit model degradation in the clean environment. Our approach is summarized in Figure 1.

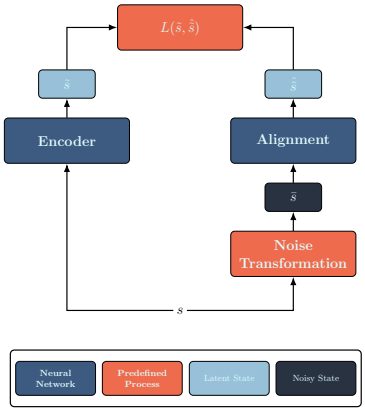

Figure 1: Overview for training the alignment model given a latent space encoder and noise transformation that applies to states to which the world model and heuristic function should be invariant.

2 Related Work

Model-based reinforcement learning and planning. Model-based RL (MBRL) improves sample efficiency by learning a dynamics model and exploiting that model for policy improvement or planning [8]. Dyna architecture interleaves real experience with model-generated rollouts to update value functions and policies [8]. More recent methods couple learned neural models with powerful search procedures. AlphaZero learns value and policy networks and performs Monte Carlo Tree Search (MCTS) in known perfect-information games [9], while MuZero achieves superhuman performance without access to the true simulator by learning a latent dynamics model for planning with MCTS [10]. PlaNet, Dreamer, and DreamerV2 learn latent world models and optimize policies via latent imagination, but they do not perform explicit test-time search to arbitrary goal states [11, 12, 13]. In contrast to policy-only use of models, our setting requires long-horizon search guided by a learned heuristic over representations that support exact state re-identification.

Learning state representations for search. A body of work learns symbolic or latent state spaces that enable classical search from pixels. LatPlan learns a discrete binary latent representation with an autoencoder and induces a classical planning model solvable by off-the-shelf planners [14, 15]. PPGS [16] learns a continuous latent space with forward and inverse models, constructs a latent-state graph using threshold-based state re-identification, and then uses uninformed graph search to solve combinatorial puzzles. However, continuous latent rollouts can accumulate error and force frequent re-planning, and uninformed breadth-first search scales poorly [16]. A complementary line learns heuristics to guide search directly from experience. DeepCubeA trains a deep neural network to approximate the cost-to-go via deep approximate value iteration and uses the learned heuristic with A* search to solve the Rubik's Cube and other puzzles, training against a single fixed goal (the canonical solved state) [17]. DeepCubeAI [5] instead learns a discrete world model and a goal-conditioned heuristic defined over binary latent states, rounding each bit at 0.5 eliminates compounding errors in long rollouts and enables state re-identification, supporting efficient search in latent space [18]. Our work builds on this discrete-latent planning foundation but addresses robustness to observation variations by learning a lightweight alignment network, leaving the world model and heuristic unchanged.

Handling visual domain variation. Domain shift in observations (e.g., lighting, background, camera pose) challenges visual planning systems. Domain randomization broadens the training distribution in simulation so real observations appear as another randomized variant [19, 20]. In robotics, sim-to-real pipelines augment randomization with image-to-image translation, e.g., RCAN maps randomized renders to a canonical domain to improve transfer [21]. In RL specifically, data augmentation improves policy robustness [22, 23]. DARLA learns disentangled representations with beta-VAE pretraining to achieve zero-shot transfer across visual changes before learning to act [24]. Beyond training-time robustness, test-time adaptation methods update perception or policies during deployment without labels or rewards, for example PAD for self-supervised policy adaptation [25] and invariance through latent alignment (ILA), which aligns target-domain features to the source distribution without paired data [26]. These approaches, however, generally target policy performance and short-horizon control rather than long-horizon heuristic search that requires exact state re-identification. SPAR complements these lines: we isolate perception shift by learning an alignment network that maps varied observations into a fixed discrete latent space. This preserves the long-horizon stability and exact state re-identification of discrete-latent planning [5] while avoiding retraining the dynamics model or heuristic for each new visual change.

3 Preliminaries

3.1 Pathfinding

The particular kind of planning problems SPAR addresses are pathfinding problems. A pathfinding problem can be defined as a weighted directed graph [27], where nodes represent states, edges represent actions that transition between states, weights on the edges represent transition costs, a given state represents the start state, and a given set of states represents the goal. The transition function, T, defines how actions transform states, where $s' = T(s, a)$ for some action a, if and only if there exists an edge connecting state s to s'. The transition-cost function, $c(s, a)$, is the cost of taking action a in state s. While we will use the aforementioned notation throughout the rest of the paper, from a reinforcement learning perspective, a pathfinding problem can also be defined as a deterministic un-discounted Markov decision process [28]. Given a pathfinding problem, the objective is to find a sequence of actions that transforms the start state into a goal state with preference for paths with lowest cost, where the cost of a path is the sum of transition costs. The cost-to-go is the cost of a lowest cost path, also known as a shortest path.

3.2 DeepCubeAI

Training DeepCubeAI [5] learns a discrete world model represented as a deep neural network (DNN) [29] that maps states to binary latent states from an offline dataset of state, action, and next state tuples. The world model is learned using an encoder to map states to discrete latent states, a decoder that maps discrete latent states to states, and a world model that maps discrete latent states and actions to next states. The encoder and decoder are trained to minimize the reconstruction error

between the input to the encoder and the output of the decoder. Simultaneously, the encoder and world model are trained to accurately predict the next state.

After learning, the outputs of the discrete world model are rounded, which prevents model degradation when errors are less than 0.5. Using the learned world model, DeepCubeAI then learns a heuristic function represented as a deep Q-network (DQN) [30], using Q-learning [31] to estimate the cost-to-go when starting from a given state and taking a given action. Training data is obtained by using the world model to generate new experiences from the offline dataset. As a result, the heuristic function takes latent states as input.

Solving Pathfinding Problems After training, a particular pathfinding problem is given to DeepCubeAI in the form of a start state image and a goal image. DeepCubeAI then encodes the start state and goal state into the discrete latent space and uses the learned world model to perform heuristic search in the latent space, guided by the learned heuristic function, to find a path from the latent start state to the latent goal state. The heuristic search algorithm checks whether a latent state encountered during search is a goal state by checking if all bits match the latent goal state. Since the world model is represented as a DNN, using it for heuristic search can be computationally expensive. Therefore, Q* search [18], a variant of A* search [7] that uses a DQN as the heuristic function, is used to find paths. This is because, with respect to the size of the action space, the number of applications of the transition function (the world model, in this case) remains constant for each iteration in the case of Q* search as opposed to growing linearly in the case of A* search.

4 Methods

SPAR assumes a trained encoder that maps states to latent states and a trained world model that maps latent states and actions to next latent states. Given a pretrained world model, our goal is to train an alignment model that maps noisy states to their corresponding discrete latent states in the clean environment. We train this model with supervised learning on a dataset of (state, latent-state) pairs (noisy states paired with their clean discrete latent states) minimizing mean squared error (MSE) between the model output and the target latent state. To gather training data, we reuse the dataset originally used for the world model, applying some transformations with random intensities, that introduces perturbations to which the world model and heuristic function should be invariant. This transformation can be applied either to states in the offline dataset or to new states sampled from the environment, if the original dataset is not available.

4.1 Discrete World Model

We map pixel observations into a discrete latent space and learn transitions within it. Let E be the encoder, D the decoder, and T the transition model. Encoder outputs pass through a logistic layer and are rounded to {0,1}, and a straight-through estimator [32] is used to enable gradient-based training.

From offline pairs (s_i, a_i, s'_i), we optimize two losses. First, a reconstruction loss to ensure meaningful encodings and decodings, given in equation 1.

$$L_r(\theta) = \frac{1}{N} \sum_{i=1}^{N} \left(\frac{1}{2} \left\| s_i - D\big(E(s_i)\big) \right\|_2^2 + \frac{1}{2} \left\| s'_i - D\big(E(s'_i)\big) \right\|_2^2 \right) \tag{1}$$

Second, a transition loss coupling encoder and transition outputs. With rounded. Denote the rounded encoder codes by $r(\tilde{s}_i) = r\big(E(s_i)\big)$ and $r(\tilde{s}'_i) = r\big(E(s'_i)\big)$, and the transition prediction by $\hat{\tilde{s}}'_i = T(\tilde{s}_i, a_i)$. We minimize the loss given in equation 2.

$$L_m(\theta) = \frac{1}{N} \sum_{i=1}^{N} \left[\frac{1}{2} \left\| r(\tilde{s}'_i) - r(\hat{\tilde{s}}'_i).detach() \right\|_2^2 + \frac{1}{2} \left\| r(\tilde{s}'_i).detach() - \hat{\tilde{s}}'_i \right\|_2^2 \right] \tag{2}$$

4.2 Alignment Model

Given a pretrained (E, T, D) learned in a clean setting, we train an alignment network A that maps a visually transformed input $\bar{s}$ to the corresponding discrete latent of the clean observation $\hat{\tilde{s}} = E(s)$. Training data are constructed as pairs of (variant observation, base observation) by aligning variant frames with their corresponding base frames at the same time step within each episode. We use supervised learning to train A by minimizing the mean squared error between the alignment network's raw (unrounded) outputs and the discrete latent targets (the encoder's rounded outputs). During the inference we round the outputs of the alignment network $A(\bar{s})$. Formally, with $\hat{\tilde{s}} = A(\bar{s})$ and the target $\tilde{s} = E(s)$, the loss is $\|\hat{\tilde{s}} - \tilde{s}\|_2^2$.

Visual variations. To probe visual robustness, we apply a series of perturbations to the images of Rubik's Cube and Sokoban. Forin pre-render (background), object-render (lighting, color, geometry), and post-render stages. Additionally, we apply object-level and background transformations to Rubik's Cube, such as color shifts and calibrations, sticker wear, material finish, camera viewpoint changes and zoom, and a physically-motivated directional lighting model [33, 34, 35, 36, 37]. Backgrounds used for Rubik's Cube included images from CIFAR dataset [38], selected randomly. These transformations were applied with parameters sampled per-frame to cover a wide range of observation changes. The transformations are explained in Appendix B along with their example figures. However, we use combinations of these individual transformations for Rubik's Cube and, both combinations and individual augmentations for Sokoban. Figure 2 is an example of the data in our dataset.

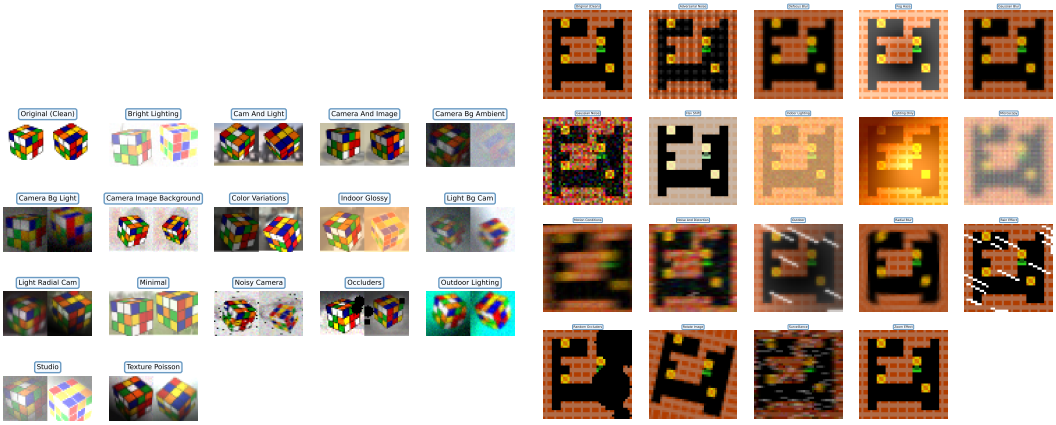

Figure 2: Visualization of sample data from the datasets used for training the alignment model for Rubik's Cube and Sokoban

5 Experiments

We evaluate SPAR, isolating the role of discrete latents and the alignment network in long-horizon planning. Below we detail the experimental setup, models, training procedures, and evaluation framework. For, world model training and heuristic learning, we use the a similar setup as DeepCubeAI with the same underlying logic and implementation as their publicly available codebase [39].

5.1 Experimental Setup

Domain. We consider visual path-finding domains with deterministic dynamics and discrete action spaces. Our primary domain is $3 \times 3 \times 3$ Rubik's Cube. We generate offline datasets of episodes by random action policies constrained to valid moves. We use quarter-turn metric (QTM) to measure solution cost, where each 90-degree face turn has unit cost. The action space has 12 actions, one for each face and direction. States are represented as 32×32 RGB images.

Offline datasets. For training the world model and heuristic function, we generate an offline dataset of 10,000 episodes using action sequences of 30 steps, sampled uniformly at random from the valid

move set. Then we use 90% of the dataset for training and 10% for validation. Start states are sampled by applying 100–200 inverse moves from the canonical solved configuration, ensuring diverse but reachable states. Moreover, we generate a dataset of 100 episodes and 10,000 steps for comparing rollout stability between discrete and continuous models. For training the alignment model, we generate a dataset of 10,000 episodes and 30 steps for per each visual variant of the environment by applying random transformations to states in the original dataset, and we pair each transformed state with its corresponding base state. However, it is possible to use a new dataset that includes visual variations and clean images that are not present in the original dataset.

5.2 Model Architectures

Encoder, decoder, transition model, and heuristic model follows DeepCubeAI's architecture. Details of these models are given in Appendix A. For the alignment model, both for Rubik's Cube and Sokoban we use a convolutional residual architecture. The input is a 6-channel tensor which first passes through a batch normalization layer, followed by two convolutional layers. The first layer maps $6 \to 64$ channels with a 5×5 kernel, stride 2, and padding 2. The second layer maps $64 \to 36$ channels with a 3×3 kernel, stride 1, and padding 1. Both layers use batch normalization, and ReLU non-linearities. The convolutional head is followed by a residual block consisting of 12 residual blocks of 38 channels, each with batch normalization and ReLU activation. The output is then flattened and passed through a two-layer MLP of size $9216 \to 11000 \to 400$. Batch normalization and ReLU are applied after, and a sigmoid activation is used at the final layer to produce a 400-dimensional output aligned to the encoder's latent space.

5.3 Models and Training Procedures

Discrete world model. We train an encoder E, transition model T, and decoder D on base images. For Rubik's Cube, E and D were fully connected networks. E outputs a 400-dimensional vector, is then passed through a logistic function and rounded to $\{0, 1\}^{400}$. T is a four-layer MLP with 500, 500, 500, and 400 parameters respectively. Additionally, we use batch normalization and ReLU except for the final logistic outputs. Actions are one-hot encoded and concatenated to the latent representation. We train E and T jointly, minimizing the reconstruction and transition objectives in Equations 1 and 2 with a scheduler that increases the transition model's loss weight from 1×10^{-3} over time until both the encoder's loss and transition model's loss have an equal weight of 0.5. We use Adam optimizer [40] with learning rate 10^{-3}, weight decay 10^{-5}, and batch size 100. We use the same architecture for the continuous model. However, we do not round the outputs of the encoder and the transition model in this case.

Alignment model. Given a fixed (E, T, D) trained on base images, we train an alignment network A to map visually varied observations $\bar{s}$ to clean environment's discrete latents $s' = E(s)$. For training the alignment model, we use supervised learning on (variant, base) pairs, and mean-squared error $\|\hat{\tilde{s}} - \tilde{s}\|_2^2$. During inference we apply rounding to $A(\bar{s})$ to obtain discrete latent states prior to planning.

Heuristic learning. We train a goal-conditioned DQN over discrete latent using Q-learning with targets defined by the world model, and assuming unit transition costs for each action taken. Training data is synthesized by random walks in latent space via T. Actions for data generation are sampled with a Boltzmann distribution over current Q-values. Similar to to priror work, we maintain a target network and update it if greedy best-first rollouts evaluation of the DQN being trained, is improved.

5.4 Evaluation Framework

Rollout stability and reconstruction. To quantify stability, we follow the same procedure as DeepCubeAI and evaluate 100 sequences of 10,000 steps each with uniformly random actions. At every step we advanced one latent step using T and reconstruct with D, measuring: (i) reconstruction MSE, and (ii) encoder consistency MSE (between $E(s)$ and $T(s, a)$). For discrete models we also tracked exact equality rates between predicted and target latent.

Planning performance. We assess planning by mapping start and goal observations to discrete latents, using the alignment model. Then we run Q* search in discrete latent space with exact bitwise

goal tests. We report the percentage of problems solved and the cost of found solutions in Table1, and the results for each visual transformation in Table 2. We also compare the results to a greedy policy, which uses the learned heuristic to select the action with the lowest estimated cost-to-go at each step for 100 iteration.

Table 1: Comparison of SPAR (ours) with a greedy policy and DeepCubeAI on different variants of the observations along the dimension of solution length, percentage of optimal solutions, number of nodes generated, time taken to solve the problem (in seconds), number of nodes generated per second, and percentage solved.

DOMAIN	OBSERVATION	SOLVER	LEN	NODES	SECS	NODES/SEC	SOLVED
Rubik's Cube	Clean	SPAR	23.61	1.91E+05	6.18	3.10E+04	100%
		DeepCubeAI	23.61	1.91E+05	5.96	3.20E+04	100%
		Greedy Policy	–	–	–	–	0%
	Augmented	SPAR	23.64	1.91E+05	6.22	3.08E+05	89.39%
		DeepCubeAI	–	–	–	–	0%
		Greedy Policy	–	–	–	–	0%
	Real-World	SPAR	23.61	1.90E+05	6.21	3.10E.51	50%
		DeepCubeAI	–	–	–	–	0%
		Greedy Policy	–	–	–	–	0%

Model Performance. To determine the performance of the alignment model, similar to DeepCubeAI, we evaluate both models on 100 sequences of 10,000 steps each, with actions selected uniformly at random. For every step, we record the ground-truth image, advance one step in the latent space, and reconstruct the observation using the decoder. We also compare against a continuous variant that shares the same architecture and training procedure as the discrete model but omits discretization. Results, shown in Figure 3, indicate that the continuous model accumulates substantial error for Rubik's Cube. Figure 4 shows the mean squared error across 17 transformations of the environment from Rubik's Cube domain where the continuous model exhibits degradation, whereas the discrete model remains accurate.

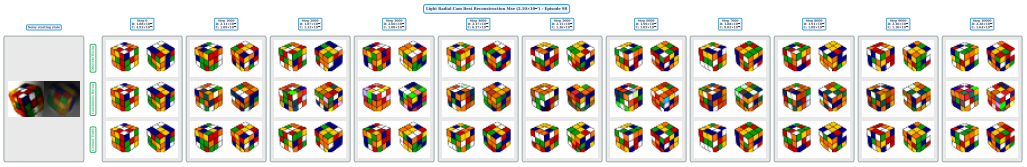

Figure 3: Reconstruction of the alignment model's outputs starting from a noisy observation of the environment.

Generalization to Unseen Variations and Real Images. To assess generalization, capabilities of SPAR, we evaluate on compositions and random intensities of transformations that were not present during alignment training. Moreover, we use the same trained alignment model to evaluate our framework on real-world data. We use photos of a Rubik's Cube taken in real-world in different lighting conditions and backgrounds. We first take two photos of Rubik's Cube in a similar orientation to the offline data. These two photos are then resized to 32×32 and concatenated horizontally. The prediction of the alignment model is then passed to the pretrained decoder to get the reconstruction of the discrete encoding (Figure 6). We compare the The discrete alignment retains strong performance when perturbations respect structural cues (e.g., moderate color shifts and lighting changes) and degrades gracefully when cues are heavily occluded or geometry is distorted. We have included examples of the variants that the search component could not find a solution for them in Figure 5 and Appendix E and real-world examples. In cases where the alignment model's output match the outputs of the encoder applied to the corresponding state in the simulation, the Q* component finds a path to given goal.

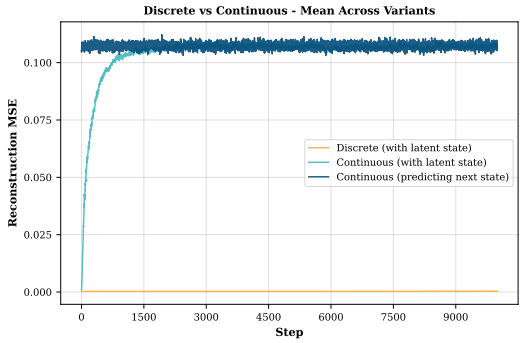

Figure 4: Mean squared error for discrete vs. continuous alignment models across Rubik's Cube variants over 10,000 steps. The label "with latent state" refers to training the continuous alignment model in the same way that the discrete model was trained. The label "predicting next state" refers to the training where the given current state and action, world model predicts next state, and the objective of alignment model is, given a visually transformed current state, to minimize the reconstruction loss between prediction of next state and the ground truth next state observed in a clean environment.

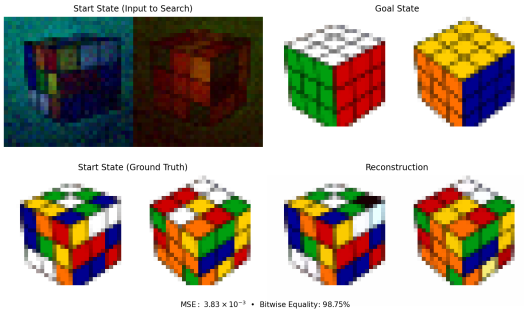

Figure 5: An example of an augmentation that SPAR fails to accurately predict the discrete latent code, and therefore is not solved during planning.

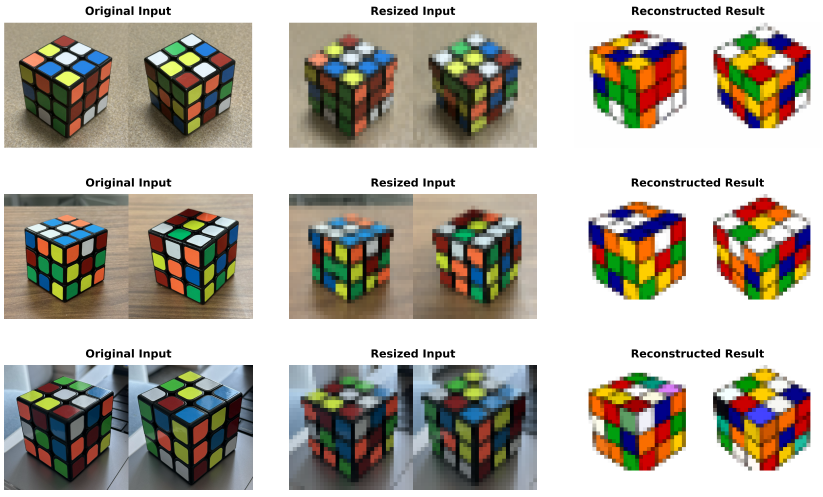

Figure 6: Applying SPAR to a real-world Rubik's Cube image with differing lighting/background.

6 Discussion

Discrete latents act as an error-correcting bottleneck for planning. Rounding removes small deviations, enabling deep rollouts without drift and precise state matching. Decoupling the encoder from dynamics learning yields practical benefits. When new variations are introduced to the environment, only re-training the alignment model is enough to leverage the benefits of the discrete world model and its quality perseverance and capabilities when used with heuristic learning and planning, while the world model and heuristic remain intact. Empirically, this substantially reduces retraining time, from days need to train a heuristic function down to a few minutes or hours, and preserves planning competence under varying visual conditions. See Section 7 for a focused discussion of data requirements and failure modes.

7 Limitations and Future Work

SPAR separates perception alignment from planning, offering a promising foundation for robust decision making. Future work can focus on extending its adaptability to richer forms of variation, enabling online learning, linking with foundation and symbolic models, and validating its utility in real-world domains. We first summarize key limitations and failure modes, and then outline directions to address them.

Reliance on paired data. A potential limitation is the reliance on paired data (i.e., a "noisy" observation and its corresponding "clean" latent representation) for training the alignment network. While feasible in simulation, acquiring such perfectly paired data in the real world can be challenging. To relax this assumption, future work can explore: (i) weakly supervised or unpaired objectives. (ii) self-training with planner consistency, where model rollouts that agree across augmentation sets provide pseudo-labels. (iii) domain adaptation and test-time adaptation to update the alignment model without labels. and (iv) leveraging foundation models to provide soft correspondences or invariance hints that regularize the alignment.

Failure cases. SPAR can fail when perturbations erase task-relevant structure (e.g., severe occlusion) or when observations fall far off the training distribution, leading to incorrect latent rounding. Detecting and mitigating these cases is an open direction: confidence estimates over discrete latents, agreement checks across augmentations, abstention or fallback policies, adversarially generated augmentations, and robust objectives could reduce brittleness and improve reliability.

Beyond deterministic, fully observable settings. Our experiments consider deterministic dynamics with fully observable states. Extending SPAR to stochastic and partially observable environments invites several avenues: (i) replace the single next-latent with a transition distribution or an ensemble to capture stochasticity; (ii) maintain a belief over discrete latents (e.g., via HMMs/particle filters or recurrent state) and train the alignment network to output observation likelihoods rather than a single code; (iii) plan in belief space using POMDP solvers or MCTS over a compact belief parameterization; and (iv) use temporal windows and predictive state representations to disambiguate aliased observations. These extensions would broaden applicability to real-world robotics and control.

Integration with Large-Scale Models. In the same vein, we envision using large vision-language models (VLMs) or large language models (LLMs) to guide planning. Complementarily, SPAR's discrete latents can be mapped to a predicate inventory and interfaced with formal goal languages specifying what must (or must not) hold, and a solver validates/grounds these targets before SPAR plans [41]. For interpretability and reuse, inductive logic programming (ILP) can be used along with SPAR's canonical states to provide human-readable rationales [42]. Incorporating multi-modal planning capabilities, e.g., specifying goals in natural language or using audio/visual cues in the environment, would broaden SPAR's applicability.

Broader Deployment Domains. Finally, applying SPAR to real-world sequential decision-making problems is an important direction. In robotics, an agent often encounters varying lighting, backgrounds, etc. SPAR could provide a fast way to recalibrate the robot's perception without retraining its policy or dynamics model each time the environment changes [43, 44]. Fast, adaptation of perception without full retraining aligns with test-time adaptation results in robotics and perception [45, 46].

Coupling SPAR with classic robot planning algorithms or continuous control techniques may be necessary to handle continuous action spaces, but the principle of a discrete latent adapter remains useful (for instance, an alignment network could map camera images to a canonical state representation on which a downstream motion planner operates).

In summary, SPAR takes a significant step toward robust model-based planning by cleanly separating the concerns of dynamics and perception. By anchoring different visual observations to a common discrete representation, it achieves long-horizon stability with minimal retraining.

8 Conclusion

Our study across different transformation families shows that this separation is practical: an alignment model alone suffices to recover planning performance while cutting retraining time by at least 95% while having the same pathfinding capabilities as DeepCubeAI. Conceptually, SPAR complements two major threads: (i) model-based RL with latent planning, where discrete latents and imagination have driven strong performance, and (ii) robustness and sim-to-real pipelines that map diverse observations into a canonical domain. By aligning into a discrete latent space and then planning with exact goal tests, SPAR maintains long-horizon stability while adapting rapidly to observation changes.

References

[1] Sébastien Racanière, Théophane Weber, David Reichert, Lars Buesing, Arthur Guez, Danilo Jimenez Rezende, Adria Puigdomenech Badia, Oriol Vinyals, Nicolas Heess, Yujia Li, et al. Imagination-augmented agents for deep reinforcement learning. In *Advances in neural information processing systems*, pages 5690–5701, 2017.

[2] Danijar Hafner, Timothy Lillicrap, Ian Fischer, Ruben Villegas, David Ha, Honglak Lee, and James Davidson. Learning latent dynamics for planning from pixels. In *International conference on machine learning*, pages 2555–2565. PMLR, 2019.

[3] Marco Bagatella, Miroslav Olšák, Michal Rolínek, and Georg Martius. Planning from pixels in environments with combinatorially hard search spaces. *Advances in Neural Information Processing Systems*, 34: 24707–24718, 2021.

[4] Stephen Tian, Suraj Nair, Frederik Ebert, Sudeep Dasari, Benjamin Eysenbach, Chelsea Finn, and Sergey Levine. Model-based visual planning with self-supervised functional distances. In *International Conference on Learning Representations*, 2021.

[5] Forest Agostinelli and Misagh Soltani. Learning discrete world models for heuristic search. *Reinforcement Learning Journal*, 4:1781–1792, 2024.

[6] Rémi Coulom. Efficient selectivity and backup operators in monte-carlo tree search. In *International conference on computers and games*, pages 72–83. Springer, 2006.

[7] Peter E Hart, Nils J Nilsson, and Bertram Raphael. A formal basis for the heuristic determination of minimum cost paths. *IEEE transactions on Systems Science and Cybernetics*, 4(2):100–107, 1968.

[8] Richard S. Sutton. Integrated architectures for learning, planning, and reacting based on approximating dynamic programming. In *Proceedings of the Seventh International Conference on Machine Learning*, pages 216–224. Morgan Kaufmann, 1990.

[9] David Silver, Thomas Hubert, Julian Schrittwieser, Ioannis Antonoglou, Arthur Guez, et al. A general reinforcement learning algorithm that masters chess, shogi, and go through self-play. *Science*, 362(6419): 1140–1144, 2018.

[10] Julian Schrittwieser, Ioannis Antonoglou, Thomas Hubert, Karen Simonyan, Laurent Sifre, et al. Mastering atari, go, chess and shogi by planning with a learned model. *Nature*, 588:604–609, 2020.

[11] Danijar Hafner, Timothy P. Lillicrap, Ian Fischer, Ruben Villegas, David Ha, Honglak Lee, and James Davidson. Learning latent dynamics for planning from pixels. In *Proceedings of the 36th International Conference on Machine Learning*, volume 97 of *PMLR*, pages 2555–2565, 2019.

[12] Danijar Hafner, Timothy P. Lillicrap, Jimmy Ba, and Mohammad Norouzi. Dream to control: Learning behaviors by latent imagination. In *International Conference on Learning Representations*, 2020.

[13] Danijar Hafner, Timothy P. Lillicrap, Mohammad Norouzi, and Jimmy Ba. Mastering atari with discrete world models. In *International Conference on Learning Representations*, 2021.

[14] Masataro Asai and Alex Fukunaga. Classical planning in deep latent space. In *Proceedings of the Thirty-Second AAAI Conference on Artificial Intelligence*, pages 6094–6101, 2018.

[15] Masataro Asai, Hiroki Yamasaki, and Alex Fukunaga. Classical planning in deep latent space: Bridging the subsymbolic-symbolic boundary. *Journal of Artificial Intelligence Research*, 75:645–704, 2022.

[16] Simone Bagatella, Evangelos Nizou, Alexandre Bizzarri, Tomasz Kornuta, Plinio Moreno, et al. Planning from pixels through graph search. In *Advances in Neural Information Processing Systems*, 2023.

[17] Forest Agostinelli, Stephen McAleer, Alexander Shmakov, and Pierre Baldi. Solving the rubik's cube with deep reinforcement learning and search. *Nature Machine Intelligence*, 1(8):356–363, 2019.

[18] Forest Agostinelli, Shahaf S Shperberg, Alexander Shmakov, Stephen McAleer, Roy Fox, and Pierre Baldi. Q* search: Heuristic search with deep q-networks. In *ICAPS Workshop on Bridging the Gap Between AI Planning and Reinforcement Learning workshop*, 2024.

[19] Josh Tobin, Rachel Fong, Alex Ray, Jonas Schneider, Wojciech Zaremba, and Pieter Abbeel. Domain randomization for transferring deep neural networks from simulation to the real world. In *2017 IEEE/RSJ International Conference on Intelligent Robots and Systems*, pages 23–30, 2017.

[20] Fereshteh Sadeghi and Sergey Levine. Cad2rl: Real single-image flight without a single real image. In *Robotics: Science and Systems*, 2017.

[21] Stephen James, Paul Wohlhart, Mrinal Kalakrishnan, Dmitry Kalashnikov, Alex Irpan, et al. Sim-to-real via sim-to-sim: Data-efficient robotic grasping via randomized-to-canonical adaptation networks. In *Proceedings of the IEEE/CVF Conference on Computer Vision and Pattern Recognition*, pages 12627–12637, 2019.

[22] Michael Laskin, Kimin Lee, Aravind Srinivas, Emile Mathieu, Zhaoping He, et al. Reinforcement learning with augmented data. In *Advances in Neural Information Processing Systems*, 2020.

[23] Denis Yarats, Ilya Kostrikov, and Rob Fergus. Image augmentation is all you need: Regularizing deep reinforcement learning from pixels. In *International Conference on Learning Representations*, 2021.

[24] Irina Higgins, Arka Pal, Andrei A. Rusu, Loic Matthey, Christopher P. Burgess, et al. Darla: Improving zero-shot transfer in reinforcement learning. In *Proceedings of the 34th International Conference on Machine Learning*, volume 70 of *PMLR*, pages 1480–1490, 2017.

[25] Nicklas Hansen, Hao Su, and Xiaolong Wang. Self-supervised policy adaptation during deployment. In *International Conference on Learning Representations*, 2021.

[26] Takuma Yoneda, Ge Yang, Vincent Sitzmann, Phillip Isola, Tsung-Yi Lin, Alexei A. Efros, and Lerrel Pinto. Invariance through latent alignment. In *Robotics: Science and Systems*, 2022.

[27] Ira Pohl. Heuristic search viewed as path finding in a graph. *Artificial intelligence*, 1(3-4):193–204, 1970.

[28] Martin L Puterman. *Markov decision processes: discrete stochastic dynamic programming*. John Wiley & Sons, 2014.

[29] Jürgen Schmidhuber. Deep learning in neural networks: An overview. *Neural networks*, 61:85–117, 2015.

[30] Volodymyr Mnih, Koray Kavukcuoglu, David Silver, Andrei A Rusu, Joel Veness, Marc G Bellemare, Alex Graves, Martin Riedmiller, Andreas K Fidjeland, Georg Ostrovski, et al. Human-level control through deep reinforcement learning. *Nature*, 518(7540):529–533, 2015.

[31] Christopher JCH Watkins and Peter Dayan. Q-learning. *Machine learning*, 8(3-4):279–292, 1992.

[32] Yoshua Bengio, Nicholas Léonard, and Aaron Courville. Estimating or propagating gradients through stochastic neurons for conditional computation. *arXiv preprint arXiv:1308.3432*, 2013.

[33] Josh Tobin, Rachel Fong, Alex Ray, Jonas Schneider, Wojciech Zaremba, and Pieter Abbeel. Domain randomization for transferring deep neural networks from simulation to the real world. In *2017 IEEE/RSJ international conference on intelligent robots and systems (IROS)*, pages 23–30. IEEE, 2017.

[34] Zhun Zhong, Liang Zheng, Guoliang Kang, Shaozi Li, and Yi Yang. Random erasing data augmentation. In *Proceedings of the AAAI conference on artificial intelligence*, volume 34, pages 13001–13008, 2020.

[35] Connor Shorten and Taghi M Khoshgoftaar. A survey on image data augmentation for deep learning. *Journal of big data*, 6(1):1–48, 2019.

[36] Dan Hendrycks and Thomas Dietterich. Benchmarking neural network robustness to common corruptions and perturbations. *arXiv preprint arXiv:1903.12261*, 2019.

[37] Longchao Da, Justin Turnau, Thirulogasankar Pranav Kutralingam, Alvaro Velasquez, Paulo Shakarian, and Hua Wei. A survey of sim-to-real methods in rl: Progress, prospects and challenges with foundation models. *arXiv preprint arXiv:2502.13187*, 2025.

[38] Alex Krizhevsky, Geoffrey Hinton, et al. Learning multiple layers of features from tiny images. 2009.

[39] Misagh Soltani. Deepcubeai: Learning discrete world models for heuristic search, 2025. URL `https://github.com/misaghsoltani/DeepCubeAI`. Commit 48a88e23fd3cfb9858552021e02545e1583aa044.

[40] Diederik P Kingma and Jimmy Ba. Adam: A method for stochastic optimization. *arXiv preprint arXiv:1412.6980*, 2014.

[41] Forest Agostinelli, Rojina Panta, and Vedant Khandelwal. Specifying goals to deep neural networks with answer set programming. In *Proceedings of the International Conference on Automated Planning and Scheduling*, volume 34, pages 2–10, 2024.

[42] Forest Agostinelli, Rojina Panta, Vedant Khandelwal, Biplav Srivastava, Bharath Chandra Muppasani, Kausik Lakkaraju, and Dezhi Wu. Explainable pathfinding for inscrutable planners with inductive logic programming. In *ICAPS 2022 Workshop on Explainable AI Planning*, 2022.

[43] Alberta Longhini, Yufei Wang, Irene Garcia-Camacho, David Blanco-Mulero, Marco Moletta, Michael Welle, Guillem Alenyà, Hang Yin, Zackory Erickson, David Held, et al. Unfolding the literature: A review of robotic cloth manipulation. *Annual Review of Control, Robotics, and Autonomous Systems*, 8, 2024.

[44] Mohan Krishna Nutalapati, Lavish Arora, Anway Bose, Ketan Rajawat, and Rajesh M Hegde. A generalized framework for autonomous calibration of wheeled mobile robots. *Robotics and Autonomous Systems*, 158: 104262, 2022.

[45] Hyoungseob Park, Anjali Gupta, and Alex Wong. Test-time adaptation for depth completion. In *Proceedings of the IEEE/CVF Conference on Computer Vision and Pattern Recognition*, pages 20519–20529, 2024.

[46] Maytus Piriyajitakonkij, Mingfei Sun, Mengmi Zhang, and Wei Pan. Tta-nav: Test-time adaptive reconstruction for point-goal navigation under visual corruptions. *arXiv preprint arXiv:2403.01977*, 2024.

[47] Volodymyr Mnih, Koray Kavukcuoglu, David Silver, Alex Graves, Ioannis Antonoglou, Daan Wierstra, and Martin Riedmiller. Playing atari with deep reinforcement learning. *arXiv preprint arXiv:1312.5602*, 2013.

A Model Architecture

Here, we detail the neural network architectures used for encoder, decoder, transition model, and heuristic model.

For Rubik's Cube, We use fully connected networks for encoder and decoder with one hidden layer, and output a 400-dimensional vector. Similarly, decoder uses fully connected networks with a linear (identity) function as the final activation. For the transition model, we use four fully connected layers of size $500 \to 500 \to 500 \to 400$ with batch normalization and ReLU, except for the last layer where we do not use batch normalization with logistic outputs. Actions are one-hot encoded and concatenated to the input state and passed to the neural network. For heuristic function, we use a deep Q-network (DQN) [47] with a fully connected residual network. The input is the concatenation of the discrete latent representations of current state and goal state. A two-layer MLP maps $800 \to 5000 \to 1000$ with batch normalization and ReLU after each layer. This is followed by 4 residual blocks of width 1000, each block having batch normalization and ReLU activation. At the final layer, a linear activation outputs Q-values for all actions $(1000 \to 12)$.

For Sokoban, we use a two-layer convolutional encoder with 2×2 kernels, stride 2, and zero paddings, mapping channels $\texttt{chan\_in} \to 16 \to 16$. Batch normalization and ReLU are applied after the first layer. The second layer uses a sigmoid activation. The resulting feature map has spatial size 10×10 with 16 channels and is flattened to a 1600-dimensional vector $(10 \times 10 \times 16)$. For transition model,

actions are one-hot encoded as channel planes and concatenated with the current latent feature maps along the channel dimension. The transition model is a 3-layer 3×3 convolutional network with stride 1 and padding 1 $(\texttt{number of actions} + 16) \to 32 \to 32 \to 16$. The first two layers use batch normalization and ReLU, and the final layer omits batch normalization and uses a sigmoid output. The decoder mirrors the encoder with two transposed 2×2 convolutions of stride 2, mapping $16 \to 16 \to 16$ channels (batch norm + ReLU on the first, sigmoid on the second) to upsample back to the original spatial resolution. A final 1×1 convolution maps $16 \to \texttt{chan\_in}$ with a linear (identity) activation to reconstruct the observation. Similar to Rubik's Cube, the DQN input is the concatenation of the encoded current state and goal state, giving a $2 \times 1600 = 3200$-dimensional vector. A two-layer MLP maps $3200 \to 5000 \to 1000$ with batch normalization and ReLU after each layer. This is followed by 4 fully connected residual blocks of width 1000, each using batch normalization and ReLU. A final linear head outputs Q-values for all actions $(1000 \to \texttt{number of actions})$.

B Appendix: Additional Rollouts and Visualizations

In this appendix we provide supplementary rollout visualizations for the discrete and continuous alignment models for the Rubik's Cube domain. Each figure block below shows: (a) a best-performing episode, (b) a worst-performing episode, and (c) a representative selected episode. All images show reconstructed frames from the alignment model's latent predictions with inputs given in the left panels. The output of the alignment model is then given to decoder for visualizing the reconstruction.

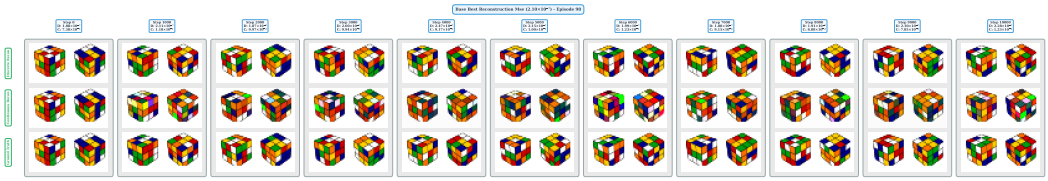

Figure 7: Reconstructions of rolling out the discrete and continuous alignment model rollouts for the Base setup. The figure shows best, worst, and representative episodes for both models in a single composite image.

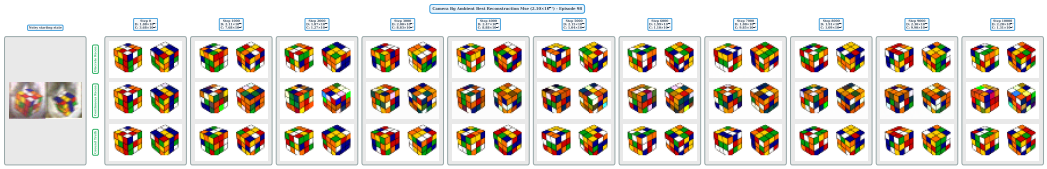

Figure 8: Reconstructions of rolling out the discrete and continuous alignment models for the Ambient Background + Camera perturbation.

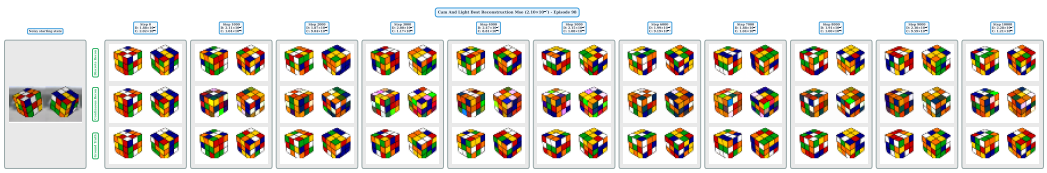

Figure 9: Reconstructions of rolling out the discrete and continuous alignment models for the Camera + Lighting perturbation.

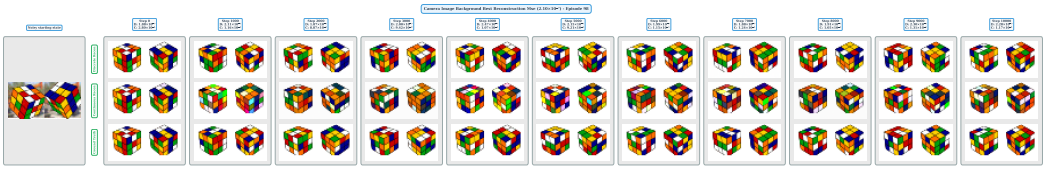

Figure 10: Reconstructions of rolling out the discrete and continuous alignment models for the Image Background perturbation.

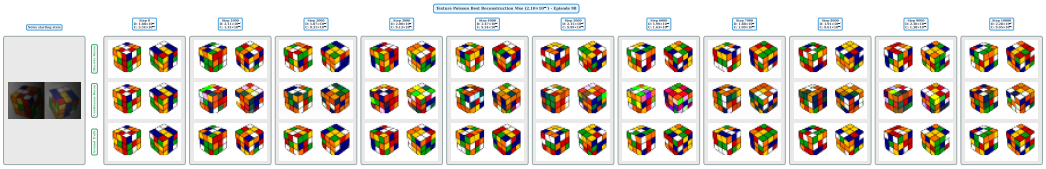

Figure 11: Reconstructions of rolling out the discrete and continuous alignment models for the Textured Background + Poisson Noise perturbation.

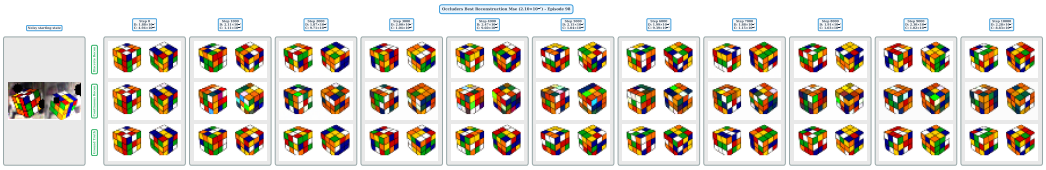

Figure 12: Reconstructions of rolling out the discrete and continuous alignment models for the Occlusions perturbation.

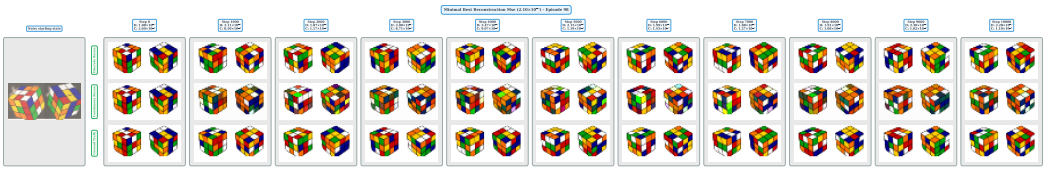

Figure 13: Reconstructions of rolling out the discrete and continuous alignment models for the Minimal Augmentations perturbation.

C Environmental Perturbation Augmentations

This appendix formalizes the augmentations used to simulate environmental perturbations in the Rubik's cube environment. For each augmentation, we state the governing principle, outline the methodology of application, specify controlling parameters and their qualitative effects. We denote an image by $I : \Omega \subset \mathbb{R}^2 \to [0,1]^3$ with per-channel intensities in $[0,1]$. Elementwise operations act per pixel and per channel unless noted. $\mathrm{clip}(\cdot)$ truncates to $[0,1]$. Convolution is $*$. Homogeneous image coordinates are $\tilde{\boldsymbol{x}} = (x, y, 1)^\top$.

Directional Surface Lighting (Lambertian) Per-surface intensity follows a Lambertian model augmented with ambient and back-face floor terms. Let $\boldsymbol{n}$ be the surface normal and $\boldsymbol{\ell}$ a unit light direction. The shading field is $S = \mathrm{clip}\left(A + (1-A)\max(0, \boldsymbol{n}\cdot\boldsymbol{\ell}) + s\right)^\gamma$, and the observed color is $\mathrm{clip}(S \odot \boldsymbol{c})$, where A is ambient, s a subsurface/back-face term, $\gamma > 0$ a contrast control, and $\boldsymbol{c}$ the base reflectance. Azimuth and elevation set $\boldsymbol{\ell}$. This augmentation represents directional illumination, self-shadowing, and highlight contrast on faceted objects.

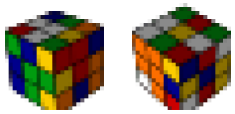

Figure 14: $A = 0.2, \kappa = 0.6, \gamma = 1.5, s = 0.1, azdeg = 315, altdeg = 45$

Random Background Chromaticity To diversify global backgrounds across frames, the constant color is drawn from a distribution, typically $\boldsymbol{c} \sim \mathcal{U}([0,1]^3)$. The rendering pipeline applies the sampled $\boldsymbol{c}$ before foreground compositing, inducing broad variation in global tone and contrast. Parameters are the sampling law and any constraints on hue or saturation. This models uncontrolled ambient lighting and incidental background coloration across capture sessions.

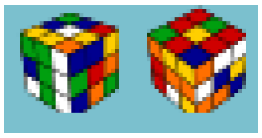

Figure 15: $\boldsymbol{c} \sim \mathcal{U}([0,1]^3)$

Procedural Background Textures A parametric texture $B(\boldsymbol{x})$ (e.g., grids, dots, stripes, noise, crosshatch, sinusoids) is synthesized in image coordinates and alpha-composited behind the object, $I' = (1-\alpha)\, I + \alpha\, B$. The construction of B governs spatial frequency, orientation, regularity, and contrast. Parameters include the texture family, spatial density, tint, and opacity $\alpha \in [0,1]$. This augmentation reproduces structured backgrounds such as patterned walls or tabletops that introduce periodic distractors and clutter.

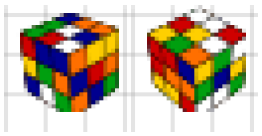

Figure 16: $B(\boldsymbol{x}) = grid, color = gray, density = 1, \alpha = 0.3$

Hue-Saturation-Value Adjustment Chromatic attributes are modified by mapping RGB to HSV, applying a hue rotation and multiplicative scaling of saturation and value, then mapping back. Writing $(h,s,v) \mapsto (h',s',v')$ with $h' = (h + \Delta_h) \bmod 1$, $s' = \mathrm{clip}(\lambda_s s)$, $v' = \mathrm{clip}(\lambda_v v)$ alters perceived colorfulness and brightness while preserving relative luminance structure. The parameters are Δ_h, $\lambda_s \geq 0$, and $\lambda_v \geq 0$. This simulates camera white-balance shifts, colored illumination, and post-processing tints.

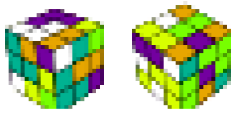

Figure 17: $\Delta_h = 0.12, \lambda_s = 1.25, \lambda_v = 1.12$

Contrast and Brightness A global affine photometric transform, $I' = \mathrm{clip}(\alpha I + \beta)$, adjusts contrast via the gain $\alpha > 0$ and brightness via the offset $\beta \in \mathbb{R}$. The method is applied uniformly per pixel and channel, followed by clipping. This models exposure settings and tone-curve changes typical of automatic image pipelines.

Figure 18: $\alpha = 1.25, \beta = 0.1$

Exposure via Gamma Nonlinear tone mapping with gamma correction redistributes mid-tones while preserving black/white after clipping: $I' = \mathrm{clip}(I^{1/\gamma})$. The parameter $\gamma > 0$ brightens ($\gamma < 1$) or darkens ($\gamma > 1$) mid-range intensities. The augmentation captures low-light and short exposure regimes.

Figure 19: $\gamma = 1.5$

Color Temperature Shift A chromatic bias along the red-blue axis emulates warm/cool illumination. In RGB, a simple model biases red and blue in opposite directions, e.g., $I'_R = \mathrm{clip}(I_R + \delta)$, $I'_B = \mathrm{clip}(I_B - \delta)$, leaving green largely unchanged. The scalar δ controls the shift magnitude. This represents tungsten (warm) versus daylight (cool) lighting and mixed color temperatures.

Figure 20: $\delta = 0.12$

Ambient Color Overlay Uniform ambient illumination is modeled by alpha-blending with a constant color: $I' = (1 - \alpha)I + \alpha\,\boldsymbol{c}$. The overlay color $\boldsymbol{c}$ and opacity $\alpha \in [0, 1]$ define the effective fill light. The result approximates global tints arising from wall reflections, skylight, or translucent enclosures.

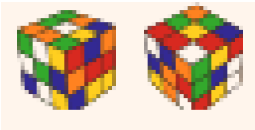

Figure 21: $\alpha = 0.2, \boldsymbol{c} = \#ffd1a4$

Directional Light with Optional Vignetting After gamma-based exposure adjustment, a directional lighting field modulates intensity according to a cosine-like pattern aligned with a unit vector $\boldsymbol{d}$ at angle θ. With normalized coordinates $\hat{\boldsymbol{x}} \in [-1, 1]^2$, the mask $m(\boldsymbol{x}) = \mathrm{clip}\big(\frac{1}{2}\hat{\boldsymbol{x}} \cdot \boldsymbol{d} + \frac{1}{2}\big)$ yields $I' = \mathrm{clip}\{I^{1/\gamma} \odot (A + \kappa m)\}$. A radial vignette $v(r) = 1 - \eta r$ optionally attenuates corners. Parameters are $\gamma > 0$, direction θ, directional strength $\kappa \geq 0$, ambient $A \in [0, 1]$, and vignette strength $\eta \in [0, 1]$. This emulates off-axis window light, desk lamps, and lens vignetting.

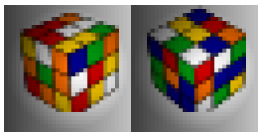

Figure 22: $\gamma = 1, \theta = 0, \kappa = 1, A = 0.5, \eta = 0.5$

In-Plane Rotation A rigid planar transform rotates the image about its center, $\boldsymbol{x}' = \mathbf{R}_\theta(\boldsymbol{x} - \boldsymbol{c}) + \boldsymbol{c}$, with resampling at inverse-warped coordinates to preserve grid spacing. The angle θ controls orientation. The augmentation models camera roll, tripod tilt, and handheld orientation drift.

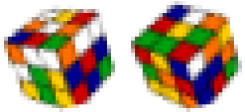

Figure 23: $\theta = 15$

Isotropic Zoom Uniform scaling by factor f about the image center modifies field of view: $f > 1$ crops the center region and upsamples. $f < 1$ downsamples and pads to original size. The single parameter $f > 0$ governs magnification. This simulates focal changes, reframing, and subject distance variation.

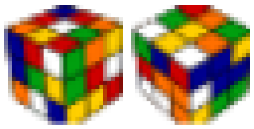

Figure 24: f=1.2

Edge Cropping with Rescaling A fraction κ of one edge is removed and the remaining content is resized back to the original dimensions, conserving aspect ratio. Parameters are the crop fraction $\kappa \in (0, 0.5)$ and the selected edge. The effect models partial occlusions, misframing, and sensor readout loss.

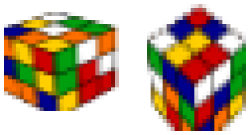

Figure 25: $\kappa = 0.2$

Additive Gaussian Noise Zero-mean i.i.d. noise is added per pixel, $I' = \text{clip}(I + \varepsilon)$, $\varepsilon \sim \mathcal{N}(0, \sigma^2)$. The standard deviation $\sigma > 0$ controls grain strength. This simulates sensor read noise and compression residue at moderate bitrates.

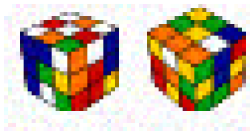

Figure 26: $\sigma = 0.05$

Salt-and-Pepper Noise Impulsive corruption sends a proportion p of pixels to intensity extremes, with salt ratio ρ governing the fraction set to white versus black. Parameters are the amount $p \in (0, 1)$ and salt ratio $\rho \in [0, 1]$. This reproduces stuck pixels, transmission dropouts, and packet loss artifacts.

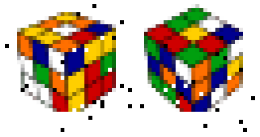

Figure 27: $p = 0.01, \rho = 0.5$

Poisson (Shot) Noise Photon-counting statistics are modeled by $I' = \frac{1}{K}\,\mathrm{Poisson}(KI)$, where K is an exposure scale. As K decreases, variance grows relative to mean, especially in dark regions. This augmentation captures low-light and short exposure regimes.

Figure 28: K=256

Multiplicative Speckle Noise Granular fluctuations modulate intensity multiplicatively: $I' = \mathrm{clip}(I \odot (1 + n))$ with $n \sim \mathcal{N}(0, \sigma^2)$. The variance σ^2 shapes speckle contrast. The effect characterizes coherent imaging artifacts (e.g., ultrasound, radar) and rough surface scatter.

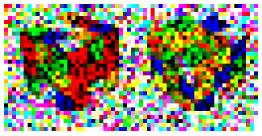

Figure 29: $n \sim \mathcal{N}(0, 1)$

Color Quantization (Banding) Uniform scalar quantization reduces the number of displayable intensities to L levels, $Q_L(I) = \frac{\lfloor LI \rfloor}{L}$. The integer $L \in [2, 32]$ sets the severity. This simulates reduced bit-depth, posterization, and banding from aggressive compression or low-quality displays.

Figure 30: L=8

Gaussian Defocus Blur Convolution with an isotropic Gaussian kernel G_σ yields $I' = G_\sigma * I$, approximating defocus from finite aperture. Separability provides efficient realization. The standard deviation $\sigma > 0$ determines blur radius. The augmentation models out-of-focus capture and depth-of-field limits.

Figure 31: $\sigma = 1.5$

Horizontal Motion Blur Apparent lateral motion is approximated by 1D convolution along the horizontal axis with a box kernel of width k, effectively averaging shifted replicas: $I' = b_k *_x I$. The kernel size k (odd) increases streak length. This simulates camera pan or fast object motion.

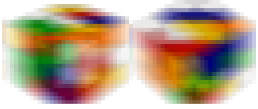

Figure 32: k=9

Radial (Spin) Blur Small-angle rotations around the image center are averaged: $I' = \frac{1}{N}\sum_{i=1}^{N} \mathcal{R}_{\theta_i}(I)$, $\theta_i \in [-\theta_{\max}, \theta_{\max}]$. Parameters are the number of rotations N and maximum angle $\theta_{\max}$. The augmentation represents rotational shake and platform yaw jitter.

Figure 33: $N = 7, \theta_{\max} = 5$

Radial Lens Distortion For normalized coordinates $\boldsymbol{u}$, a radial warp $\boldsymbol{u}' = \boldsymbol{u}\,(1 + k\|\boldsymbol{u}\|^2)$ models first-order barrel ($k < 0$) or pincushion ($k > 0$) distortion. Inverse mapping with interpolation produces the output grid. The distortion strength k controls severity. This reproduces wide-angle lens distortion and optical calibration error.

Figure 34: k=0.0001

Projective (Perspective) Transform A homography $\mathbf{H} \in \mathbb{R}^{3\times3}$ maps homogeneous coordinates via $\tilde{\boldsymbol{x}}' \sim \mathbf{H}\tilde{\boldsymbol{x}}$. Choosing $\mathbf{H}$ from perturbed corner correspondences induces keystone deformation. Inverse warping with interpolation preserves sampling density. Parameters are corner displacements or direct specification of $\mathbf{H}$. This models oblique viewpoints and camera pose changes relative to the image plane.

Figure 35: $\Delta = 0.1$

Object Albedo Channel Offset Object face colors are shifted additively in RGB, $\boldsymbol{a}' = \mathrm{clip}(\boldsymbol{a} + \boldsymbol{\delta})$, applied to each semantic region prior to shading. The channel-wise offsets control tint magnitude and direction. This emulates illumination casts and sensor biases producing uniform tints on object surfaces.

Figure 36: $\boldsymbol{\delta} = [0.1, 0, 0]$

Object Albedo Channel Scaling A diagonal color calibration $\mathbf{D} = \mathrm{diag}(\lambda_R, \lambda_G, \lambda_B)$ scales albedo channels, $\boldsymbol{a}' = \mathrm{clip}(\mathbf{D}\boldsymbol{a})$. Per-channel gains $\lambda_\cdot$ modulate relative color balance. The augmentation simulates white-balance and per-channel gain mismatches across cameras.

Figure 37: $\lambda_R = 1, \lambda_G = 1, \lambda_B = 1$

Material Fading (Sticker Wear) Chromatic content blends toward local luminance $y = \frac{1}{3}(a_R + a_G + a_B)$: $\boldsymbol{a}' = (1-\rho)\boldsymbol{a} + \rho\, y\, \mathbf{1}$. The fade factor $\rho \in [0, 1]$ governs desaturation. The effect captures sun bleaching, aging, and pigment loss from surface wear.

Figure 38: $\rho = 0.5$

Micro-Texture Perturbations High-frequency albedo perturbations are injected as bounded noise $\boldsymbol{\epsilon} \in [-\nu, \nu]^3$ added to each surface region, followed by clipping. The amplitude ν shapes scratch visibility. This simulates fine scratches and scuffs that locally modulate reflectance.

Figure 39: $\nu = 0.05$

Polygonal Imperfections in Stickers Vertices of sticker polygons receive bounded spatial jitter $\Delta\boldsymbol{v}$ with $\|\Delta\boldsymbol{v}\| \leq \epsilon$, preserving polygon closure. The piecewise-linear boundary undergoes small shape changes. The jitter radius ϵ sets deviation magnitude.

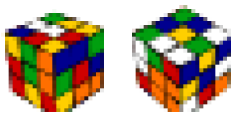

Figure 40: $\epsilon = 0.05$

Camera Pose Perturbation (Yaw-Pitch-Roll) The extrinsic rotation is varied by Euler angles (ψ, ϕ, φ), and the pinhole projection maps 3D points $\tilde{\boldsymbol{X}}$ to pixels via $\tilde{\boldsymbol{x}} \sim \mathbf{K}\,[\mathbf{R}(\psi, \phi, \varphi) \mid \boldsymbol{t}]\,\tilde{\boldsymbol{X}}$. Small perturbations in the angles capture realistic viewpoint drift while maintaining object visibility. This simulates handheld motion and mount misalignment.

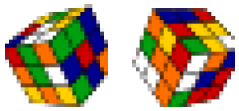

Figure 41: $\psi = -20, \phi = -10, \varphi = -8$

3D Zoom and Viewport Translation Scene geometry is uniformly scaled by s, optionally combined with a small translation within the image plane. The projection window adjusts to avoid cropping. Parameters are scale $s > 0$ and planar offsets. The effect simulates effective focal changes and subject recentering without altering the background.

Figure 42: $s = 1.2, offset_x = 0, offset_y = 0$

For Rubik's Cube, we combine these augmentations into the following variants:

- Directional lighting with controllable ambient, shadow, gradient, and subsurface components background image composited behind the cube, camera yaw, pitch, and roll.
- HSV hue, saturation, and value shifts and RGB channel offsets, global contrast and brightness scaling, zoom-in and zoom-out, and positional offsets, camera rotation, and background image.
- A lightweight mix for regularization involving directional lighting, zoom and vertical offset, camera angle variation, background image, and ambient light tint to simulate global illumination.
- Warm look with glossy material finish for the cube, slight sticker-vertex jitter, per-channel color calibration, warm ambient light and color-temperature shift, zoom and camera jitter, and a background image.
- Harsher directional light with optional vignette, color-temperature shifts in both directions, Gaussian blur and exposure gamma variation, background randomization from the image pool, camera jitter, and low to moderate additive Gaussian noise.
- High-key lighting with white ambient fill, slightly increased contrast and brightness, glossy finish, per-channel scaling, and Gaussian noise.
- Noisy surveillance look with higher Gaussian noise, salt-and-pepper noise, reduced color bit-depth (banding), edge cropping, conservative contrast tweaks, mixed matte or glossy finish, and sticker jitter.
- Controlled illumination using a white ambient fill plus directional light, glossy material, sticker jitter, low noise, slightly boosted contrast, and a background image.

- Camera angle variation, a background image, Gaussian noise to mimic sensor grain.
- Background image, camera jitter, Gaussian blur, directional light with gamma and vignette controls, and light Gaussian noise.
- Background image, directional light combined with a colored ambient wash, motion blur, and Gaussian noise.
- Similar to the above but with lighter ambient, motion blur, a milder vignette, and small Gaussian noise.
- Filled background image, Gaussian blur, radial motion blur, colored ambient light at low opacity, small Gaussian noise, and directional light with vignette.
- Procedural background texture patterns (grid, dots, stripes, crosshatch, waves, or noise) added in the background, Gaussian blur and radial blur, Poisson noise, and directional light on the cube.
- Random opaque shapes placed in front of the scene to partially occlude the cube, combined with Gaussian noise, directional light, camera jitter, zoom, and a background image.
- A simple composition of a background image, directional lighting on the cube, and camera pose variation.

D Planning Result Tables

Table 2: SPAR performance on Rubik's Cube across augmentation variants, showing solution length, percentage optimal, nodes generated, time (seconds), nodes per second, and percentage solved.

DOMAIN	OBSERVATION	LEN	NODES	SECS	NODES/SEC	SOLVED
Rubik's Cube	Bright Lighting	23.60	1.90E+05	0.21	8.95E+05	95.3%
	Camera and Background and Ambient Light	23.66	1.91E+05	0.21	8.94E+05	77.4%
	Camera and Background and Lighting	23.62	1.91E+05	0.25	7.60E+05	89%
	Camera and Background Image	23.59	1.90E+05	0.21	8.95E+05	96.7%
	Camera and Background Image	23.61	1.91E+05	0.27	6.94E+05	96.6%
	Camera and Lighting	23.61	1.91E+05	0.20	9.44E+05	96.7%
	Color Variations	23.60	1.90E+05	0.24	7.85E+05	92.6%
	Indoor and Glossy	23.64	1.91E+05	0.23	8.42E+05	96.5%
	Lighting and Radial Blur and Camera	23.64	1.91E+05	0.25	7.67E+05	88.9%
	Lighting and Background and Camera	23.64	1.92E+05	0.23	8.37E+05	79.3%
	Minimal	23.61	1.91E+05	0.28	6.91E+05	97.6%
	Noisy Camera	23.61	1.91E+05	0.24	7.91E+05	89.8%
	Occluders	23.74	1.93E+05	0.24	8.18E+05	78.3%
	Outdoor Lighting	23.75	1.93E+05	0.27	7.17E+05	71.1%
	Studio	23.58	1.91E+05	0.30	6.29E+05	75.9%
	Texture and Poisson Noise	23.62	1.91E+05	0.31	6.07E+05	94.1%

E Unsolved Examples

In this section we include some examples of the test instances that were not solved during planning. These examples show the significant changes in the observations during augmentation.

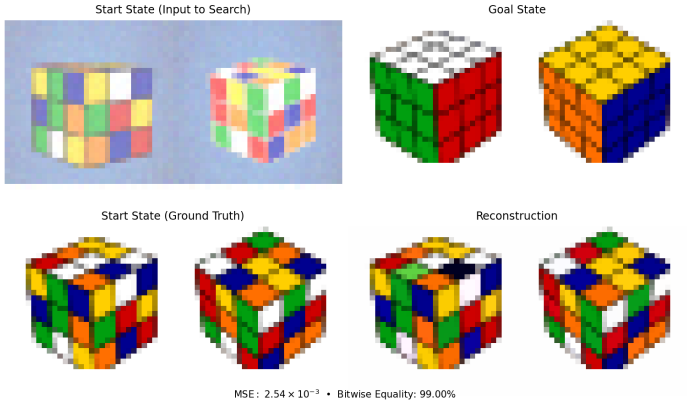
Start State (Input to Search)
Goal State
Start State (Ground Truth)
Reconstruction
MSE: 2.54×10^{-3} • Bitwise Equality: 99.00%

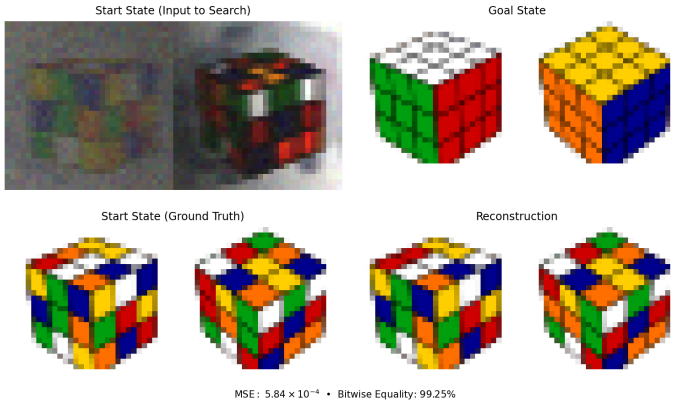
Start State (Input to Search)
Goal State
Start State (Ground Truth)
Reconstruction
MSE: 5.84×10^{-4} • Bitwise Equality: 99.25%